

Potential Dependence of Nitrate Adsorption and Dissociation across Metals and Dilute Alloys: a Grand Canonical Study

Dean M. Sweeney, Bolton Tran, and Bryan R. Goldsmith*

Department of Chemical Engineering, University of Michigan, Ann Arbor, MI

E-mail: bgoldsm@umich.edu

Abstract

Aqueous nitrate (NO_3^-) can be converted to value-added or benign products via electrocatalytic nitrate reduction (ENR). Although transition metal and single-atom alloy (SAA) electrocatalysts have been studied for ENR, the impact of applied electrochemical potentials on key ENR reaction steps is poorly understood. This work uses explicit grand-canonical density functional theory (eGC-DFT) and analytical grand-canonical density functional theory (aGC-DFT) to study the potential dependence of key mechanistic steps in ENR on pure metals and Cu-based SAAs. First, we predict using eGC-DFT that the (111) facets of Pd_1Cu , Ni_1Cu , Ru_1Cu , and Rh_1Cu are stable/meta-stable against surface segregation and aggregation in the presence of adsorbates, regardless of the applied potential. Studying the stable/metastable SAAs as well as pure metals with aGC-DFT, we find that the electrosorption valencies for NO_3^- adsorption vary between $-0.60 \frac{\text{eV}}{\text{V}}$ to $-0.80 \frac{\text{eV}}{\text{V}}$ across the studied catalysts. Furthermore, Cu-based SAAs behave similarly to pure metals, where the electrosorption valency correlates with the partial charge transfer from NO_3^- to the surface and trends

with the d -band filling of the metal. The predicted symmetry factors for NO_3^* dissociation to nitrite indicate a small potential dependence for this activation free energy ($-0.04 \frac{\text{eV}}{\text{V}}$ to $-0.20 \frac{\text{eV}}{\text{V}}$ across all catalysts). We show that for NO_3^- adsorption over $\text{Ni}_1\text{Cu}(111)$, a promising SAA catalyst for ENR, errors range between 5.9 kJ/mol to 61.9 kJ/mol at -0.55 V when using the Computational Hydrogen Electrode model instead of aGC-DFT. For NO_3^* dissociation over Ni_1Cu , errors range between 3.8 kJ/mol to 51.1 kJ/mol at -0.55 V vs SHE when neglecting the potential dependence altogether. However, these errors vary with the assumed electrochemical double-layer properties and the studied catalysts. Overall, this work clarifies the potential dependence of nitrate adsorption and dissociation across SAAs and pure metals, as well as demonstrates the importance of considering EDL effects.

Introduction

Electrocatalytic nitrate reduction (ENR) is being widely studied because of its potential to convert nitrate (NO_3^-) waste into value-added or benign products such as ammonia or dinitrogen.^{1,2} ENR uses electricity to drive an electrocatalyst and reduce aqueous NO_3^- through several proton-coupled-electron-transfer (PCET) steps.² Both experimental and computational studies have identified electrocatalysts that promote key reaction pathways and product formation, including pure transition metals and bimetallic alloys.² Promising electrocatalysts in terms of activity and selectivity often include platinum group elements, such as palladium (Pd), platinum (Pt), and rhodium (Rh), as well as coinage metals, such as copper (Cu).^{3,4}

More recently, single atom alloys (SAAs), a class of catalysts in which one metal element is atomically dispersed in another metal host, have demonstrated improved performance over their pure metal and bimetallic alloy counterparts.^{5–12} SAAs can potentially have high activity, high selectivity, and low cost compared to other alloys and pure metals.^{10,13–17} Particularly due to the low cost and abundance of Cu, there has been interest in Cu-based SAAs to promote electrochemical reactions such as ENR, including Ti_1Cu , Ni_1Cu , Nb_1Cu , Pd_1Cu

and Au_1Cu .^{6,8,9,11,12,18} These SAAs have been shown to promote strong NO_3^- adsorption and subsequent reduction to both dinitrogen and ammonia.

Despite the application of SAA and pure metal electrocatalysts, the impact of applied electrochemical potentials on key ENR reaction steps is not well understood, as well as the influence of dilute alloying on the potential dependence. Thus far, most theoretical studies of ENR use canonical Density Functional Theory (DFT) modeling combined with simplified approaches to consider the effects of the applied electrochemical potential on reaction energetics.^{3,18,19} The most common approach is the computational hydrogen electrode (CHE) model.¹⁹ Within the CHE framework, the adsorption energy, calculated via canonical DFT, is shifted by the electrochemical potential of the transferred electrons.¹⁹ As a result, the potential dependence of any PCET step is linearly proportional to the predetermined number of transferred electrons. For example, assuming NO_3^- adsorption is a PCET step (see eq. (1)), then the CHE model predicts an electrosorption valency of $-1.0 \frac{\text{eV}}{\text{V}}$ (i.e., the rate of change in NO_3^- adsorption energy with the applied potential).¹⁹



A major drawback of the CHE model is that it can only approximate the potential dependence of PCET reaction steps, limiting its application to a subset of reaction steps within ENR. Furthermore, it neglects the formation of counter-charge above an electrode, termed the Helmholtz Layer (used synonymously with electrochemical double layer (EDL) in this work).^{20–22} Consideration of both PCET and non-PCET reaction steps as well as EDL effects aligns closer to experimental ensembles and gives a more accurate depiction of reaction energetics in electrochemical reactions.^{23,24}

Recently, Grand Canonical DFT (GC-DFT) calculations have been used to simulate constant potential reactions and EDL effects at the electrochemical interface through computing the grand free energy.^{20,25–28} The grand free energy of a candidate structure (e.g., adsorbed nitrate), Φ_G , is shown in eq. (2), where F is the Helmholtz free energy of the system, μ_e is

the electrochemical potential of an electron, and N_{exc} is the number of excess electrons (net surface charge) to shift the system from its potential of zero charge (PZC) to the potential on the absolute scale, U .

$$\Phi_{\text{G}} = F - \mu_e N_{\text{exc}}, \quad \mu_e = -eU \quad (2)$$

An explicit GC-DFT method (eGC-DFT), such as that proposed by Sundararaman et al., computes Φ_{G} directly by changing N_{exc} to converge μ_e to $-eU$.²⁹ Ions present within the implicit solvation model simulate a collection of counter-charge above the surface and maintain overall charge neutrality. Therefore, an eGC-DFT structure optimization accounts for structural changes under applied potentials by optimizing a system with some net surface charge.

eGC-DFT methods have been used to simulate the potential dependence of CO adsorption, CO reduction, and anion adsorption, revealing appreciable EDL effects and potential dependencies.^{30–32} Alsunni et al. also found that the explicit GC-DFT yields significantly different reaction pathways and computed energetics than the CHE model for CO₂ reduction to CO.³³ To help design electrocatalysts that break adsorbate scaling relations, Gao et al. performed eGC-DFT calculations to simulate NO₃[−] reduction to ammonia over Cu(111) and Cu(100) at 0.0 V vs. the Reversible Hydrogen Electrode. However, besides the analysis by Gao et al., eGC-DFT calculations have scarcely been applied to study ENR. One limitation of eGC-DFT that hinders its more widespread use to reactions like ENR is the increased computational cost when converging an additional self-consistent loop such that $\mu_e = -eU$.

The higher computational cost of eGC-DFT can be circumvented by approximating Φ_{G} using a second-order Taylor expansion of F around the PZC, as shown in eq. (3). Here, $F(N_{\text{exc}} = 0)$ represents the ground-state energy of the candidate structure at the PZC, U_{χ} .³⁴ The second-order approximation, given in eq. (4), is derived by applying Janak’s Theorem, $\frac{\partial F}{\partial N_{\text{exc}}}|_{N_{\text{exc}}=0} = -eU_{\chi}$, along with the relation $\frac{\partial^2 F}{\partial N_{\text{exc}}^2}|_{N_{\text{exc}}=0} = \frac{e^2}{C}$, where C denotes the double-layer capacitance.³⁵ Additionally, $F(N_{\text{exc}} = 0)$ is rewritten as the DFT-computed

ground-state energy of the system at the PZC, $F_{\text{DFT}}(U_\chi)$. Using this approximation for F , the net surface charge can be determined by minimizing Φ_G with respect to N_{exc} , as shown in eq. (5).^{34,35} Substituting eq. (5) into eqs. (2) and (4) results in a quadratic approximation of Φ_G , given in eq. (6). Guo et al. utilized eq. (6) to model the potential dependence of ENR reaction mechanisms across different facets of Cu.³⁶ However, this approximation alone neglects electric field interactions present within the double layer.

$$F(N_{\text{exc}}) = F(N_{\text{exc}} = 0) + \left. \frac{\partial F}{\partial N_{\text{exc}}} \right|_{N_{\text{exc}}=0} (N_{\text{exc}}) + \frac{1}{2} \left. \frac{\partial^2 F}{(\partial N_{\text{exc}})^2} \right|_{N_{\text{exc}}=0} (N_{\text{exc}})^2 + O(N_{\text{exc}}^3) \quad (3)$$

$$F(N_{\text{exc}}) = F_{\text{DFT}}(U_\chi) - eU_\chi N_{\text{exc}} + \frac{e^2}{2C} (N_{\text{exc}})^2 + O(N_{\text{exc}}^3) \quad (4)$$

$$N_{\text{exc}} = \arg \min_{N_{\text{exc}}} (\Phi_G) = -C(U - U_\chi) \quad (5)$$

$$\Phi_G(U) = F_{\text{DFT}}(U_\chi) - \frac{C}{2} (U - U_\chi)^2 \quad (6)$$

Argawal et al. parameterized C using a parallel plate model and modified eq. (6) to account for such electric field interactions within the EDL.³⁷ As shown in eq. (7), this modification included dipole-field and induced-dipole field interactions parameterized through the surface normal dipole moment and the polarizability. In this model, U_χ and μ_χ represent the PZC and surface normal dipole moment of either a bare surface ($\chi = *$) or a surface with adsorbates ($\chi = A^*$). However, the polarizability, α_χ , represents just the adsorbate molecule ($\alpha_A = \alpha_{A^*} - \alpha_*$). Other parameters include the solution permittivity, ε , the double layer thickness, d and the surface area, A . They also provided an accurate and convenient way to compute U_χ in a dielectric medium, as shown in eq. (8), where U_0 is the PZC of the bare surface calculated in vacuum from the work function.³⁷

$$\Phi_G(U) = F_{\text{DFT}}(U_\chi) - \underbrace{\frac{1}{2} \frac{\varepsilon A}{d} (U - U_\chi)^2}_{\text{Capacitative energy}} + \underbrace{\mu_\chi \left(\frac{U - U_\chi}{d} \right)}_{\text{Dipole-field interactions}} + \underbrace{\frac{\alpha_\chi}{2} \left(\frac{U - U_\chi}{d} \right)^2}_{\text{Induced dipole-field interactions}} \quad (7)$$

$$U_\chi = U_0 + \frac{\mu_\chi}{\varepsilon A} \quad (8)$$

Overall, this analytical approach, herein referred to as aGC-DFT, presents a computationally efficient method to approximate Φ_G by optimizing the candidate structure at the PZC and then correcting the computed energy for EDL effects and applied potentials. Wong et al. demonstrated its efficacy in approximating potential-dependent activation energies of C-H, O-H, and OC-CO bond formations over Cu(111). The model maintained mean absolute errors (MAEs) between 0.03–0.06 eV compared to eGC-DFT calculations.³¹ Cui et al. also used the model to support their experimental findings that CO₂ reduction has potential-dependent negative fractional reaction orders at high overpotentials with respect to CO partial pressures.³⁸

Despite the recent widespread usage of GC-DFT applications in electrocatalysis, advanced analytical models such as eq. (7) have not been applied yet to study the potential dependence of electrochemical reactions in ENR. Furthermore, the lack of clarity regarding how different computational approaches (eGC-DFT, aGC-DFT, and CHE) diverge in their predicted energetics for other reactions underscores the need for a systematic comparison. This is especially true given that GC-DFT methods are highly sensitive to the choice of EDL parameters, including ε_r and d .^{31,39} Altogether, an analysis which outlines the applications of GC-DFT models to ENR reaction steps would provide crucial insights into the potential-dependent reaction energetics of ENR and ultimately improve the reliability of computational predictions in ENR.

Herein, we use eGC-DFT and aGC-DFT to examine the potential dependence of key steps of ENR on Cu-based SAAs, and we compare these results against pure metals. To ensure

we study likely stable SAAs, we use eGC-DFT to compute the segregation and aggregation energetics of (111) facets for eight Cu-based SAAs at -0.114 and -0.714 V vs SHE. Pd_1Cu is stable against surface segregation and aggregation across all conditions while Ni_1Cu , Ru_1Cu , and Rh_1Cu maintain positive or near-zero segregation energies with low to moderate aggregation energies, especially in the presence of adsorbed hydrogen and nitrate. When studying NO_3^- adsorption and dissociation over $\text{Cu}(111)$, we find the analytical method approximates grand free energies comparable with the explicit method. Therefore, using this analytical method, we elucidate the potential dependence of NO_3^- adsorption and dissociation over (111) and (100) facets of four SAAs and five pure metals. Our results demonstrate the shift in dipole moment dictates the potential dependence for nitrate adsorption and dissociation for both pure metals and SAAs. When neglecting EDL effects of such reactions, we demonstrate errors in calculated reaction energetics vary drastically across catalysts and with the assumed EDL properties. Ni_1Cu , our best performing SAA in terms of stability and activity towards nitrate adsorption and dissociation, has a maximum error of 13.5 kJ/mol for NO_3^- adsorption and 8.9 kJ/mol for NO_3^* dissociation at a ϵ_r of 78.4 (water), d of 3 Å, and common operating potential of -0.55 V vs SHE.

Results

Dopant Segregation and Aggregation

Before examining the effect of the applied electrochemical potential on the ability of SAAs to promote NO_3^- adsorption and dissociation, we evaluated their thermodynamic stability under applied potentials. SAAs suffer from stability problems under reaction conditions when the dopant atom segregates into the bulk structure or aggregates (clusters) with other dopant atoms on the surface, as illustrated in Figure 1a.^{17,40} While dopant segregation and aggregation are well-studied under vacuum conditions,^{40–43} the effects of adsorbates under electrochemical conditions on the segregation and aggregation of the dopant atom are

underexplored. Therefore, we analyzed the stability of eight Cu-based SAAs—Ti₁Cu, Nb₁Cu, Ni₁Cu, Ru₁Cu, Rh₁Cu, Pd₁Cu, Pt₁Cu, and Au₁Cu—because of their demonstrated activity towards ENR.^{11,18,31}

Figure 1a details the calculation of the segregation and aggregation grand free energies of the dopant atom for a bare surface ($\Delta\Phi_{\text{seg}}(U)$ and $\Delta\Phi_{\text{agg}}(U)$)⁴⁰ or in the presence of common ENR adsorbates, H* and NO₃* ($\Delta\Phi_{\text{seg}}^{\text{A}*}(U)$ and $\Delta\Phi_{\text{agg}}^{\text{A}*}(U)$). For each condition, single-atom dopants with endothermic segregation and aggregation energies are defined as stable. Unstable dopants are classified by their segregation and aggregation tendencies, depending on which one is more exothermic. All energies are eGC-DFT-computed electronic energies, absent of any entropic contributions.⁴⁰ We used the eGC-DFT method within the Joint Density Functional Theory (JDFTx) Software with the Revised Perdew-Burke-Ernzerhof (RPBE) Functional.^{29,44} The grand free energies are computed at -0.714 and -0.114 V versus SHE (common operating range of ENR). The absolute potential, U is converted to the Standard Hydrogen Electrode scale via $U = -U_{\text{SHE}} - \phi_{\text{ref}}$, where $\phi_{\text{ref}} = 4.66$ V. In this work, U automatically implies the SHE scale. Solvent and ion effects were accounted for with the CANDLE implicit solvation model. Thermochemistry corrections beyond those included within the implicit solvation model were excluded when computing the segregation and aggregation energies according to the methodology of Darby et al.⁴⁰ More information on modeling parameters and the equations for computing segregation and aggregation energies can be found in the supplementary information (SI).

In the absence of adsorbates, only Pd₁Cu, Pt₁Cu, and Au₁Cu prefer to stay as SAAs based on the thermodynamics of SAA dopant segregation ($\Delta\Phi_{\text{seg}}(U) > 0$) and aggregation ($\Delta\Phi_{\text{agg}}(U) > 0$), as shown in Figure 1b. Ti₁Cu, Ni₁Cu, and Rh₁Cu have small $\Delta\Phi_{\text{seg}}(U)$ and $\Delta\Phi_{\text{agg}}(U)$ with values between -20 kJ/mol and 13 kJ/mol only. Nb₁Cu and Ru₁Cu both have exothermic $\Delta\Phi_{\text{seg}}(U)$ and $\Delta\Phi_{\text{agg}}(U)$ indicating thermodynamic preferences for dimers.

For most of the SAAs, the applied potential has a negligible effect on the segregation and aggregation thermodynamics without adsorbates. However, Ti₁Cu and Nb₁Cu have non-

negligible variations in their $\Delta\Phi_{\text{seg}}(U)$ with the applied potential. Both Wang et al. and Gupta et al. demonstrated partial +1 charges on Ti and Nb dopants, which we confirmed (see SI), due to electron transfer with the Cu host.^{18,45} These positively charged dopants become increasingly unstable as the surface is negatively charged at -0.714 V vs SHE.

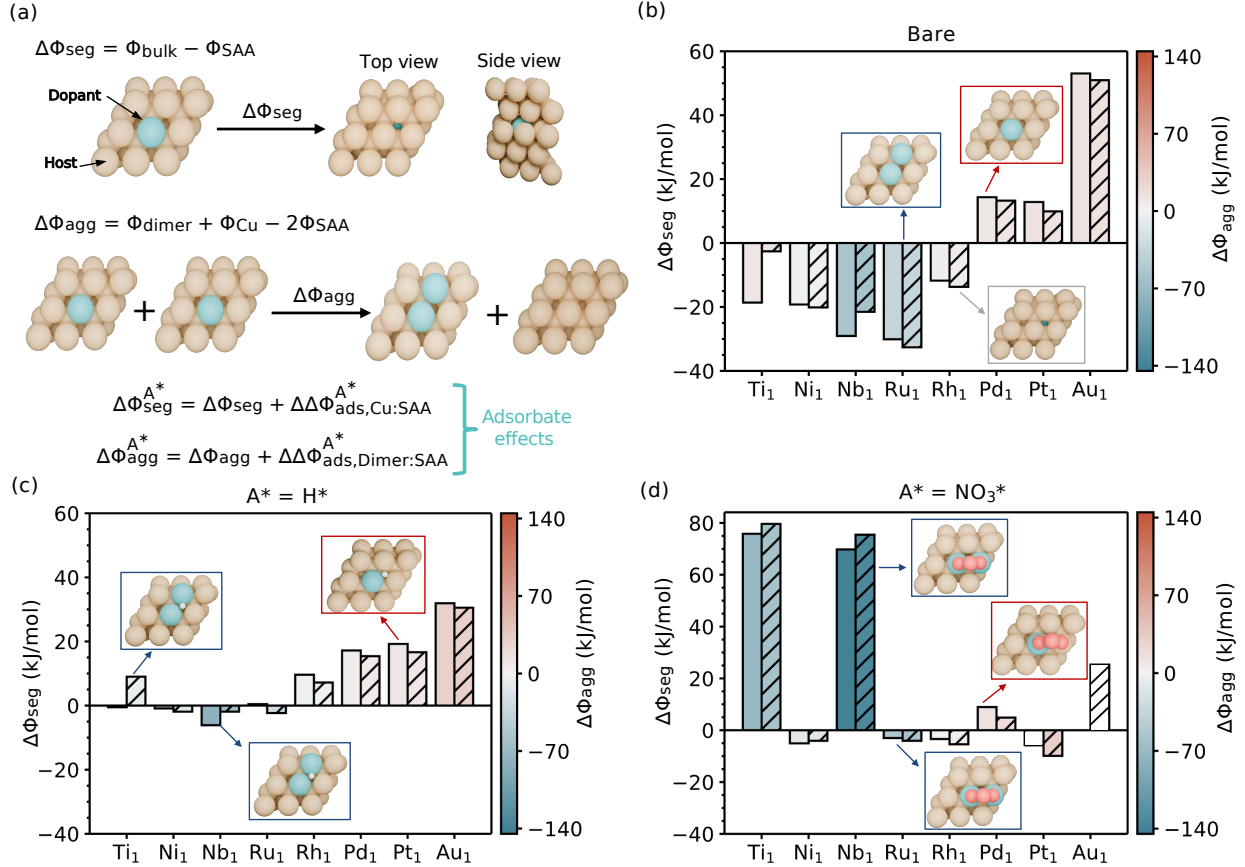


Figure 1: (a) Schematic showing dopant segregation (top) and aggregation (bottom) over a bare $\text{X}_1\text{Cu}(111)$ surface, along with the equations to compute bare surface segregation and aggregation grand free energies, $\Delta\Phi_{\text{seg}}(U)$ and $\Delta\Phi_{\text{agg}}(U)$, as well as adsorbate-induced segregation and aggregation grand free energies, $\Delta\Phi_{\text{seg}}^{\text{A}^*}(U)$ and $\Delta\Phi_{\text{agg}}^{\text{A}^*}(U)$. Here, $\Delta\Delta\Phi_{\text{ads},1:2}^{\text{A}^*}$ is the adsorption-free energy difference between system 1 and system 2. Segregation and aggregation free energies for 8 Cu-based SAAs with (b) a bare surface, (c) adsorbed hydrogen (H^*), and (d) adsorbed nitrate (NO_3^*). Segregation free energy is indicated by the bar value, where values above zero signify stability on the surface. Aggregation free energy is indicated by the bar color, where values above zero signify stability as a single dopant. Free energies were calculated at -0.114 V and -0.714 V (striped) using the eGC-DFT method. For NO_3^- adsorption on Pt_1Cu and Au_1Cu , the white colored bars or the absence of any bar indicate that NO_3^- would not adsorb on the site. The schematics in each figure show the expected SAA structure depending on the sign of the segregation and aggregation free energies.

The data in Figure 1c shows that adsorbed hydrogen makes the segregation free energy of the dopant more endothermic ($\Delta\Phi_{\text{seg}}^{\text{H}^*}(U) > \Delta\Phi_{\text{seg}}(U)$) for all SAAs except $\text{Au}_1\text{Cu}(111)$, resulting in positive or near zero values at both potentials (<10 kJ/mol). Compared to adsorption on a pure Cu surface, H^* binds more strongly on Ti_1Cu through Pt_1Cu SAAs but weaker on Au_1Cu . The preference of H^* to bind to the dopant over Cu explains why it stabilizes most dopants against segregation (compared to their bare surfaces). Conversely, H^* makes the aggregation free energy of these dopants slightly more exothermic. However, Ti_1Cu , Ni_1Cu , Rh_1Cu , Pd_1Cu , and Pt_1Cu maintain relatively small $\Delta\Phi_{\text{agg}}(U)$ with values between -15 kJ/mol and 10 kJ/mol only. Nb_1Cu and Ru_1Cu maintain their thermodynamic preferences for dimers.

As with H^* , NO_3^* induces stability on the surface when it interacts with the dopant site more strongly than with a pure Cu site. That is the case for Ti_1Cu , Nb_1Cu , Ni_1Cu , Ru_1Cu , Rh_1Cu , and Pd_1Cu , where $\Delta\Phi_{\text{seg}}^{\text{NO}_3^*}(U)$ are positive or near-zero. Conversely, NO_3^* interacts with Pt and Au more weakly than Cu, which destabilizes Pt_1Cu with $\Delta\Phi_{\text{seg}}^{\text{NO}_3^*}(U) < 0$. NO_3^* adsorbed on Pt dimers only and Au single atom sites only at -0.114 V vs SHE, indicating its preference to adsorb to pure Cu sites.

As for aggregation tendencies in the presence of NO_3^* , Pd_1Cu maintains its stability against surface aggregation while Ni_1Cu , Rh_1Cu , and Ru_1Cu have $\Delta\Phi_{\text{agg}}^{\text{NO}_3^*}(U)$ between -0.20 kJ/mol (Rh_1Cu) and -60 kJ/mol (Ru_1Cu). Ti_1Cu and Nb_1Cu have highly exothermic $\Delta\Phi_{\text{agg}}^{\text{NO}_3^*}(U)$ with values between -60 kJ/mol and -140 kJ/mol due to their strong interaction with NO_3^* . Refer to the SI for DFT-optimized structures of NO_3^* interacting with the different SAAs.

Overall, Pd_1Cu is stable against surface segregation and aggregation across all conditions. Ni_1Cu , Ru_1Cu , and Rh_1Cu maintain positive or near-zero segregation energies with low to moderate aggregation energies, especially in the presence of adsorbed H^* and NO_3^* . While Pt_1Cu and Au_1Cu maintain stability across most conditions, they adsorb NO_3^* weakly, indicating that NO_3^* may bind to pure Cu sites rather than the dopant sites. Both Ti_1Cu and

Nb₁Cu show large tendencies to cluster around NO₃*. Therefore, we only considered the performance of stable and potentially meta-stable SAAs for nitrate adsorption and dissociation, including Ni₁Cu, Ru₁Cu, Rh₁Cu, and Pd₁Cu.

Nitrate Adsorption

When NO₃⁻ adsorbs onto an electrode, it is expected to donate at least some its charge to the metal surface, which has been shown through cyclic voltammetry experiments.⁴⁶ However, the extent of the charge transfer, defined as the electrosorption valency, is unknown both computationally and experimentally. Typically, the CHE model is used to evaluate the potential dependence of this PCET step, which assumes a full electron donation upon adsorption. To address the validity of this assumption, we computed how the adsorption free energy of NO₃⁻ ($\Delta\Phi_{\text{ads}}^{\text{NO}_3^*}(U)$) changes with the applied potential through eq. (9), where $\Phi_{\text{NO}_3^*}(U)$ is the grand free energy of the surface with nitrate adsorbed and $\Phi^*(U)$ is the grand free energy of the surface without adsorbates. We modeled this adsorption as a PCET reaction step referenced to gaseous HNO₃ (see SI for the full thermodynamic cycle). G_{HNO_3} and G_{H_2} are the Gibbs free energies of gas phase HNO₃ and H₂.

$$\Delta\Phi_{\text{ads}}^{\text{NO}_3^*}(U) = \Phi_{\text{NO}_3^*}(U) - \left(\Phi_{\text{slab}}(U) + G_{\text{HNO}_3} - \frac{1}{2}G_{\text{H}_2} \right) - eU + 0.480 \quad (9)$$

We computed $\Delta\Phi_{\text{ads}}^{\text{NO}_3^*}(U)$ and the electrosorption valency for this reaction step in three ways: (1) using the CHE model and approximating $\Phi_{\text{NO}_3^*}(U)$ and $\Phi^*(U)$ with energies computed at their respective PZCs ($U_{\text{NO}_3^*}$, U_*); (2) using aGC-DFT to approximate $\Phi_{\text{NO}_3^*}(U)$ and $\Phi^*(U)$; and (3) using eGC-DFT to compute $\Phi_{\text{NO}_3^*}(U)$ and $\Phi^*(U)$ exactly. For aGC-DFT, we derived eq. (10) by substituting eq. (7) for $\Phi_{\text{NO}_3^*}(U)$ and $\Phi^*(U)$. In this model, $U'_\chi = U - U_\chi$, which is the shift from the PZC of a bare surface ($\chi = *$) or a surface with NO₃* ($\chi = \text{NO}_3^*$) to U . We assumed a double layer thickness of 3 Å and a relative permittivity (ε_r) of 78.4 (water). The absolute permittivity is computed through $\varepsilon = \varepsilon_r\varepsilon_0$,

where ε_0 is the vacuum permittivity. To compute energies at the PZC for the CHE model and the aGC-DFT method, we used the Vienna Ab Initio Simulation Package (VASP) with the RPBE functional and VASPSol continuum solvation model to simulate solvent and ion effects.⁴⁷ To compute grand free energies with the eGC-DFT method, we used JDFTx with similar settings (exchange-correlation functional, energy cutoff) as used in VASP. See the supplementary information for more information on the modeling parameters, including thermochemistry corrections to the computed free energies.²⁹

$$\begin{aligned} \Delta\Phi_{\text{ads}}^{\text{NO}_3^*}(U) = & \underbrace{\Delta\Phi_{\text{ads}}^{\text{NO}_3^*}(U_{\text{NO}_3^*}, U_*) - U}_{\text{CHE model}} - \underbrace{\frac{1}{2} \frac{\varepsilon A}{d} \left((U'_{\text{NO}_3^*})^2 - (U'_*)^2 \right)}_{\text{Capacitative energy}} \\ & + \underbrace{\mu_{\text{NO}_3^*} \left(\frac{U'_{\text{NO}_3^*}}{d} \right) - \mu_* \left(\frac{U'_*}{d} \right) + \frac{\alpha_{\text{NO}_3}}{2} \left(\frac{U'_{\text{NO}_3^*}}{d} \right)^2}_{\text{Electric-field interactions}} \end{aligned} \quad (10)$$

We first considered the potential dependence of NO_3^- adsorption over Cu(111), one of the most well-studied catalysts for ENR. Predictions of $\Delta\Phi_{\text{ads}}^{\text{NO}_3^*}(U)$ using the three different approaches within a range of -1.0 to 1.0 V are shown in Figure 2a. We note that the eGC-DFT curve is shifted upwards in energy by less than 0.1 eV compared to the aGC-DFT model predictions. We found the difference in implicit solvation methods used within JDFTx versus VASPSol causes this small deviation.

The electrosorption valencies (m) are represented by the slope of each line in Figure 2a, that is the explicit ($m_{\text{eGC-DFT}}$) and analytical ($m_{\text{aGC-DFT}}$) models predict similar electrosorption valencies of $-0.58 \frac{\text{eV}}{\text{V}}$ and $-0.69 \frac{\text{eV}}{\text{V}}$. The CHE model always predicts an electrosorption valency (m_{CHE}) of $-1.00 \frac{\text{eV}}{\text{V}}$ for one full electron transfer assumed upon adsorption. Given the agreement between the aGC-DFT and eGC-DFT results, we concluded that (1) the analytical model can approximate grand free energies reasonably well compared to the eGC-DFT method and (2) the CHE model overpredicts the potential dependence of NO_3^- adsorption

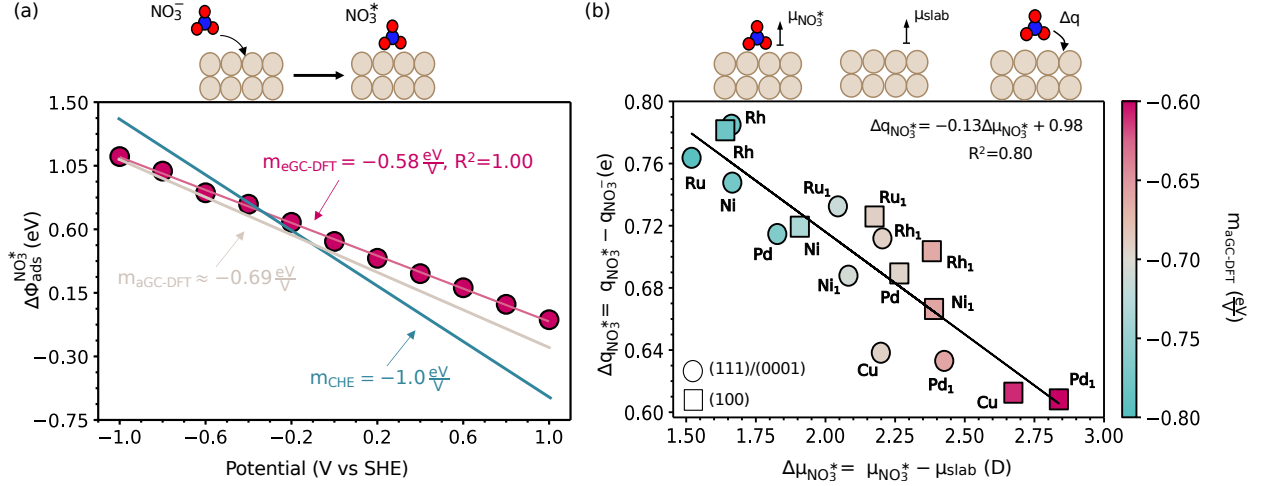


Figure 2: (a) NO_3^- adsorption energy ($\Delta\Phi_{\text{ads}}^{\text{NO}_3^*}(U)$) versus the potential on Cu(111), calculated based on the computational hydrogen electrode model (CHE), the analytical GC-DFT model (aGC-DFT), and explicit GC-DFT (eGC-DFT). Electrodesorption valencies (m_i) are written inset. The eGC-DFT model is represented by a line of best fit to free energies computed at select potentials, whereas the CHE and aGC-DFT models are continuous representations of $\Delta\Phi_{\text{ads}}^{\text{NO}_3^*}(U)$. (b) The change in surface normal dipole moment from NO_3^- adsorption ($\Delta\mu_{\text{NO}_3^*}$) versus the partial charge transfer from NO_3^- to the surface ($\Delta q_{\text{NO}_3^*}$) of different pure metals and SAAs. The color bar indicates the electroadsorption valency. Circles represent the (111) and (0001) facets, and squares represent the (100) facet. X_1Cu SAAs are labeled inset as X_1 .

for Cu(111) (i.e., $|m_{\text{CHE}}| > |m_{\text{eGC-DFT}}|, |m_{\text{aGC-DFT}}|$).

To analyze the source of the potential dependence, we derived an expression for the electroadsorption valency through the 1st-order derivative of eq. (10), shown in eq. (11). As shown, the electroadsorption valency is a function of both the change in the surface dipole moment upon adsorption, $\Delta\mu_{\text{NO}_3^*}$, the polarizability of the adsorbate, α_{NO_3} , and U_0 (as well as double layer properties). Although eq. (11) states that $\Delta\Phi_{\text{ads}}^{\text{NO}_3^*}(U)$ is nonlinear ($\frac{\partial\Delta\Phi_{\text{ads}}^{\text{NO}_3^*}(U)}{\partial U} = f(U)$), the data in Figure 2a shows a linear potential dependence, indicating that $\Delta\mu_{\text{NO}_3^*}$ controls the potential dependence over Cu(111) (i.e., $2\Delta\mu_{\text{NO}_3^*} \gg \frac{\alpha_{\text{NO}_3}}{d}$). Under this simplification, the electroadsorption valency then is only a function of $\Delta\mu_{\text{NO}_3^*}$ and the assumed double layer thickness.

$$\frac{\partial \Delta \Phi_{\text{ads}}^{\text{NO}_3^*}(U)}{\partial U} = \underbrace{\underbrace{-1}_{\text{CHE}} + \frac{2\Delta\mu_{\text{NO}_3^*}}{d} + \frac{\alpha_{\text{NO}_3}}{d^2} \left(U - U_0 - \frac{\mu_{\text{NO}_3^*}}{\varepsilon A} \right)}_{\text{aGC-DFT}} \quad (11)$$

Results from aGC-DFT for NO_3^- adsorption across (111) and (100) facets of pure metals and the identified stable/meta-stable SAAs further support the correlation between shifts in dipole moment and electrosorption valencies. Although we only studied the stability of (111) facets of the Cu-based SAAs, we also included the (100) facets to examine facet effects on the potential dependence. Shown by the color bar in Figure 2b, the electrosorption valencies for each metal ranged between $-0.60 \frac{\text{eV}}{\text{V}}$ and $-0.80 \frac{\text{eV}}{\text{V}}$, which also deviate from the CHE model prediction of $-1.00 \frac{\text{eV}}{\text{V}}$ for all metals. A combination of factors, including (1) electron redistribution on the surface due to Pauli repulsion between the adsorbate and surface electrons, (2) the intrinsic dipole moment of the molecule, and (3) partial charge transfer between the adsorbate and the surface, can influence $\Delta\mu_{\text{NO}_3^*}$, and hence the electrosorption valency.^{48–52} In the case of anion adsorption, this process is expected to be dominated by partial charge transfer from NO_3^- to the surface.

To determine whether the potential dependence of NO_3^- adsorption is driven by partial charge transfer, we used the Density Derived Electrostatics and Chemical Charges (DDEC6) atomic population analysis to compute the residual charge on NO_3^* and the partial charge transfer from NO_3^- to the surface upon adsorption, $\Delta q_{\text{NO}_3^*}$.⁵³ As shown in Figure 2b, $\Delta q_{\text{NO}_3^*}$ ranges between 0.60e^- and 0.80e^- across metals and correlates directly with $\Delta\mu_{\text{NO}_3^*}$. This indicates that NO_3^- retains some of its negative charge upon adsorption and that increased $\Delta q_{\text{NO}_3^*}$ yields smaller $\Delta\mu_{\text{NO}_3^*}$ and thus greater potential dependencies (i.e., $\uparrow |\Delta q_{\text{NO}_3^*}|$, $\downarrow |\Delta\mu_{\text{NO}_3^*}|$, $\uparrow |m_{\text{aGC-DFT}}|$).

From Figure 2b, it is apparent that non-noble metals, such as Ru, Rh, and Ni, have greater $\Delta q_{\text{NO}_3^*}$ than more noble metals, such as Cu and Pd. SAAs also have varying potential dependencies with their values generally being a weighted average of the electrosorption valencies/charge transfer of the pure Cu host and of the pure dopant surface. To relate this

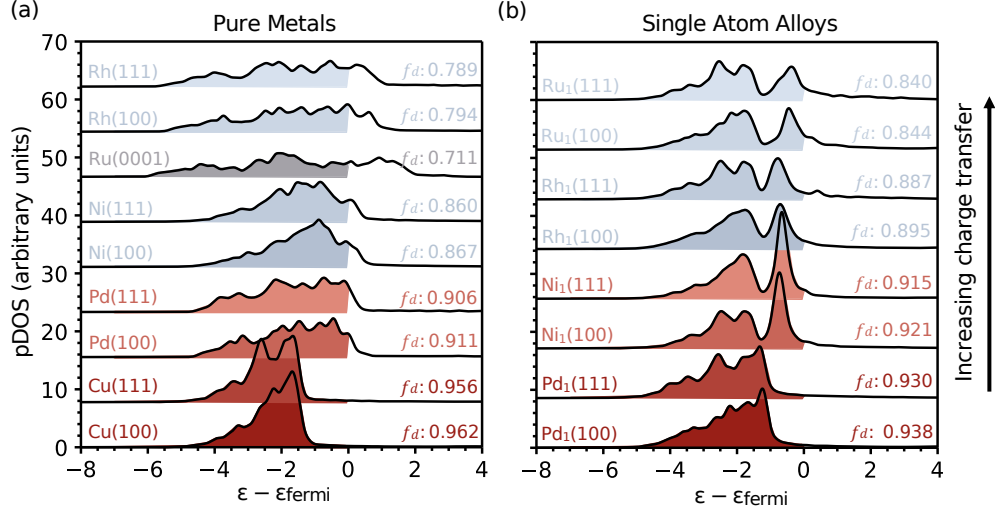


Figure 3: Partial Density of States for (a) pure metals and (b) single-atom alloys. Unshaded regions above 0.0 eV represent the unoccupied states of the metal.

behavior to metal properties, we correlated $\Delta q_{\text{NO}_3^*}$ with the d -band filling of each metal, f_d , computed from the partial density of states (pDOS) of the two atoms bound to NO_3^* . As the d -band center of the metal approaches the system's Fermi energy and the d -band width increases, the number of unoccupied states (shown by the unshaded region above 0 eV) increases. As shown in Figure 3, this effect results in lower f_d and thus greater charge transfer to the metal atoms. Therefore, metals with lower f_d , such as Ru, Rh, and Ni, have greater potential dependencies and $\Delta q_{\text{NO}_3^*}$ than Cu and Pd. Additionally, (111) facets of the same metal have greater potential dependencies than (100) facets, which have slightly larger f_d .

The SAAs also follow these nobility trends in electrosorption valencies, with their behavior modulated by the Cu host. However, their behavior is well predicted by f_d of the pure metals comprising the alloy. Larger differences in the f_d of pure Cu and that of a pure dopant atom yield a smaller SAA f_d , and thus increased charge transfer to the surface. For example, Ru(0001) and Cu(111) have the greatest difference in their pure metal f_d values (0.24 eV) and thus Ru₁Cu pulls the most charge off NO_3^- than the other SAAs. Overall, when this partial charge transfer is a prominent indicator of the electrosorption valency, as shown for

NO_3^- adsorption, this metal property explains the trends in the potential dependence across transition metals and SAAs.

Nitrate Dissociation

Next, we considered the potential dependence of NO_3^* dissociation to $\text{NO}_2^* + \text{O}^*$ over Cu(111). Typically, this reaction is assumed to have no potential dependence because there is no PCET and the CHE model fails to capture the potential dependence of such reactions. To assess this assumption, we computed how the activation energy for direct N-O bond cleavage ($\text{NO}_3^* \rightarrow \text{NO}_2^* + \text{O}^*$) changes with applied electrochemical potential through eq. (12), where $\Phi^\ddagger(U)$ is the transition state grand free energy.

$$\Delta\Phi^\ddagger(U) = \Phi^\ddagger(U) - \Phi_{\text{ads}}^{\text{NO}_3^*}(U) \quad (12)$$

As before, we assess the potential dependence of $\Delta\Phi^\ddagger(U)$ using three models. Firstly, we neglect the potential dependence by approximating $\Phi_{\text{ads}}^{\text{NO}_3^*}(U)$ and $\Phi_*(U)$ with energies computed at their respective PZCs (U_*, U_\ddagger). We then used the aGC-DFT method to approximate $\Phi_{\text{ads}}^{\text{NO}_3^*}(U)$ and $\Phi_*(U)$ through eq. (7) and the eGC-DFT method to compute $\Phi_{\text{ads}}^{\text{NO}_3^*}(U)$ and $\Phi_*(U)$ exactly. For the aGC-DFT method, we modeled $\Delta\Phi^\ddagger(U)$ through eq. (13). Unlike eq. (10), this expression includes an additional polarizability term for both the transition state and the initial state, as both contain adsorbates. All calculations were converged with the Climbing Image Nudge Elastic Band method within a force tolerance of $0.05 \frac{\text{eV}}{\text{\AA}}$. Refer to the SI for more information on model parameters, including thermochemistry corrections.

$$\begin{aligned}
\Delta\Phi^\ddagger(U) = & \Delta\Phi^\ddagger(U_\ddagger, U_{\text{NO}_3^*}) - \underbrace{\frac{1}{2} \frac{\varepsilon A}{d} \left((U_\ddagger')^2 - (U_{\text{NO}_3^*}')^2 \right)}_{\text{Capacitive Energy}} \\
& + \underbrace{\mu_\ddagger \left(\frac{U_\ddagger'}{d} \right) - \mu_{\text{NO}_3^*} \left(\frac{U_{\text{NO}_3^*}'}{d} \right) + \frac{\alpha_\ddagger}{2} \left(\frac{U_\ddagger'}{d} \right)^2 - \frac{\alpha_{\text{NO}_3}}{2} \left(\frac{U_{\text{NO}_3^*}'}{d} \right)^2}_{\text{Electric-field Interactions}}
\end{aligned} \quad (13)$$

Figure 4a shows the three predictions of $\Delta\Phi^\ddagger(U)$ within a range of -1.0 to 1.0 V. Neglecting the potential dependence yields a constant activation energy of 0.45 eV or 43.42 kJ/mol. Naturally, the analytical method predicts the same activation energy at the PZC but with a slope, referred to as the symmetry factor ($m_{\text{aGC-DFT}}$), of $-0.17 \frac{\text{eV}}{\text{V}}$. This is considerably closer to the symmetry factor predicted by the explicit method ($m_{\text{eGC-DFT}} = -0.24 \frac{\text{eV}}{\text{V}}$).

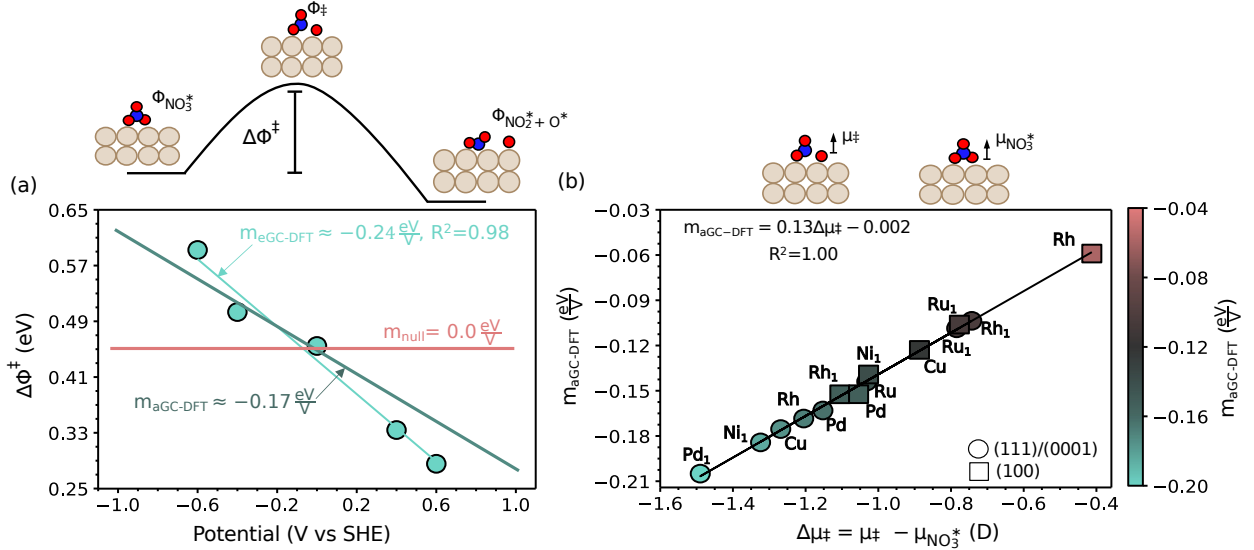


Figure 4: (a) Activation free energy for NO_3^- dissociation ($\Delta\Phi^\ddagger(U)$) versus the potential, calculated using aGC-DFT or eGC-DFT. The activation barrier computed at the pzc is also shown (red line, m_{null}). (b) The change in the surface normal dipole moment from NO_3^* to the transition state ($\Delta\mu_\ddagger$) versus the symmetry factor ($m_{\text{aGC-DFT}}$). Circles represent the (111) and (0001) facets, and squares represent the (100) facets. X_1Cu SAAs are labeled inset as X_1 .

As we observed for NO_3^- adsorption over Cu(111), $\Delta\Phi^\ddagger(U)$ is linear with U . From the first-order derivative of eq. (13), shown in eq. (14), the linear fit to the aGC-DFT method

indicates that $\Delta\mu_{\ddagger}$ controls the potential dependence for dissociation over Cu(111) (i.e., $2\Delta\mu_{\ddagger} \gg \frac{\alpha_{\ddagger}}{d}, \frac{\alpha_{\text{NO}_3^-}}{d}$). Additionally, the potential dependence of this NO_3^- dissociation step is approximately a third of the electrosorption valency for NO_3^- adsorption ($-0.17 \frac{\text{eV}}{\text{V}}$ versus $-0.58 \frac{\text{eV}}{\text{V}}$). This signifies that NO_3^- dissociation induces less of a dipole moment shift across the reaction coordinate (i.e., $|\Delta\mu_{\ddagger}| < |\Delta\mu_{\text{NO}_3^*}|$).

$$\frac{\partial\Delta\Phi^{\ddagger}(U)}{\partial U} = \frac{2\Delta\mu_{\ddagger}}{d} + \frac{\alpha_{\ddagger}}{d^2} \left(U - U_0 - \frac{\mu_{\ddagger}}{\varepsilon A} \right) - \frac{\alpha_{\text{NO}_3^-}}{d^2} \left(U - U_0 - \frac{\mu_{\text{NO}_3^*}}{\varepsilon A} \right) \quad (14)$$

The data in Figure 4b demonstrates that these findings hold across the pure metals and SAAs analyzed in this work. Symmetry factors range between $-0.04 \frac{\text{eV}}{\text{V}}$ and $-0.20 \frac{\text{eV}}{\text{V}}$ with larger $|\Delta\mu_{\ddagger}|$ yielding greater potential dependencies for the dissociation step (i.e., $|m_{\text{aGC-DFT}}| > 0$). The potential dependence of this reaction step is much lower in magnitude than the electrosorption valencies from Figure 2 with no significant trends across metal nobility or facets. Furthermore, trends in the symmetry factors of the SAAs are not well understood by examining the potential dependence or properties of the pure metals.

Errors in Neglecting EDL Effects and Model Sensitivity

To conclude this study, we quantified approximate errors in neglecting EDL effects by using just the CHE model for NO_3^- adsorption and neglecting the potential dependence altogether for NO_3^* dissociation for different catalysts and EDL parameters. Overall, this portion aims to further inform the modeling community about the errors associated with typical assumptions used for atomistic modeling of electrocatalytic reactions, as well as the sensitivity of GC-DFT results on the EDL parameters.

Across all studied SAAs, $\text{Ni}_1\text{Cu}(111)$ is moderately stable against surface segregation and aggregation (see Figure 1), adsorbs NO_3^- moderately (-22.48 kJ/mol at PZC), and cleaves the N-O bond with a relatively low dissociation barrier (46.30 kJ/mol at PZC). The stability and activity of $\text{Ni}_1\text{Cu}(111)$ and $\text{Ni}_1\text{Cu}(100)$ towards ENR have also been outlined through

both experimental research and canonical DFT modeling.^{8,12,54} Therefore, we focus here on Ni SAAs on Cu.

The computed errors for Ni₁Cu(111), Ni₁Cu(100), and Cu(111) are shown in Figures 5a and 5b, where colored lines in each plot represent the computed errors at a relative permittivity of 78.4 (water) and double layer thickness of 3 Å. Constraining the potential between -0.60 and 0.20 V to align with typical operating ranges of ENR over Cu catalysts. Ni₁Cu(111) has a maximum error of 13.5 kJ/mol for NO₃⁻ adsorption and 8.9 kJ/mol for NO₃^{*} dissociation at -0.6 V. Copper has almost identical maximum errors while Ni₁Cu(100) has maximum errors of just 10.7 kJ/mol and 5.0 kJ/mol at -0.6 V. All catalysts obtain a minimum error of 0.0 kJ/mol within the operating range of ENR.

Within each figure, there is an expression for the potential at which neglecting EDL effects results in an error of 0.0 kJ/mol (U_{\min}), i.e., where the CHE model agrees with GC-DFT. This U_{\min} is a function of the bare surface PZC, U_0 , as well as a term that shifts the PZC from U_0 due to the presence of surface normal dipole moments. This indicates that potentials near the PZC of the metal should minimize the error in neglecting EDL effects, which is typically assumed in studies using the CHE model.³⁴ However, if the adsorbates induce large surface normal dipole moments, this approximation can break down and yield significant errors in computed energetics. Nonetheless, Cu(111) and Ni₁Cu(111) have almost identical U_{\min} because of the similar PZCs between the surfaces ($U_{0, \text{Cu(111)}} = -0.090$ V, $U_{0, \text{Ni}_1\text{Cu(111)}} = -0.085$ V) while Ni₁Cu(100)'s error curve is shifted to the left with smaller maximum errors because of its smaller PZC ($U_{0, \text{Ni}_1\text{Cu(100)}} = -0.30$ V).

As the potential dependence and computed grand free energies are sensitive to the assumed double-layer properties, we also generated heat maps for the computed errors across various ϵ_r and d for Ni₁Cu(111), shown in Figures 5c and 5d. We completed this analysis at -0.55 V, the potential at which Cai et al. experimentally studied Ni₁Cu for ENR.¹² Although, Cai et al. operated on the Reversible Hydrogen Electrode scale, the pH shift to convert to the SHE scale will cancel out when computing the errors between the two models.

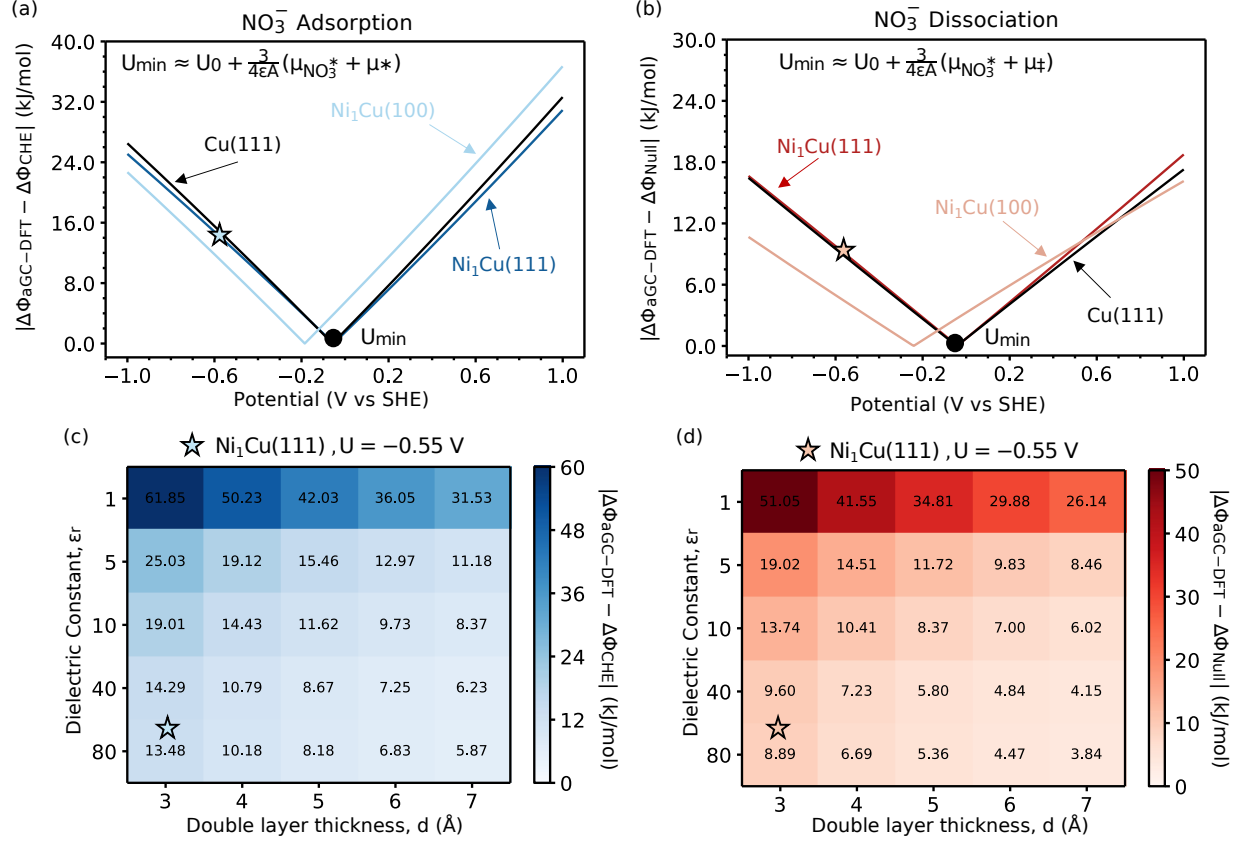


Figure 5: Approximate errors for $\text{Ni}_1\text{Cu}(111)$, $\text{Ni}_1\text{Cu}(100)$, and $\text{Cu}(111)$ from (a) computing the adsorption free energy of nitrate ($\Delta\Phi_{\text{ads}}^{\text{NO}_3^*}(U)$) with the CHE model versus the aGC-DFT method, and (b) computing the activation free energy for nitrate dissociation ($\Delta\Phi^\ddagger(U)$) with no potential dependence versus the aGC-DFT method. Errors at each potential were computed with a relative permittivity (ϵ_r) of 78.4 (water) and double layer thickness (d) of 3.0 Å. The star indicates the potential at which we considered the variations in errors with double layer properties for Ni_1Cu while U_{min} is the potential at which the error is minimized for Ni_1Cu . A heat map of computed error at -0.55 V for (c) nitrate adsorption and (d) nitrate dissociation, showing the variation in the computed errors with relative permittivity (ϵ_r) and double layer thickness (d). The stars represent the error computed with a ϵ_r of 78.4 (water) and d of 3.0 Å.

For nitrate adsorption and dissociation, errors are < 7 kJ/mol for large ϵ_r and d , but exponentially increase as ϵ_r and d decrease. The error from CHE model exceeds 60 kJ/mol for NO_3^- adsorption and 50 kJ/mol for NO_3^* dissociation at a relative permittivity of 1 (vacuum) and a double layer thickness of 3 Å. Under the range considered, aGC-DFT computed $\Delta\Phi_{\text{ads}}^{\text{NO}_3^*}(U)$ ranges between -50.85 kJ/mol and 5.14 kJ/mol and aGC-DFT computed

$\Delta\Phi^\ddagger(U)$ ranges between -52.63 kJ/mol and 99.84 kJ/mol. Referring to the derived equation for computing the error (see SI), it is trivial to observe that the only contributions to the error come from the capacitive energy to charge the double layer and the electric field interactions. Specifically, as d and ε_r approach infinity, the capacitive energy and the electric field interactions become negligible. However, a medium with a small ε_r minimally screens electric field interactions while the energy to charge a double layer becomes extensive with small d . Overall, in the regime of small ε_r and d , there are large contributions from these energy terms to computed grand free energies which should not be neglected. Based on these results and the uncertainty in EDL parameters, it is strongly recommended to consider EDL effects in computed reaction energetics to avoid significant errors.

Conclusions

Knowledge of the potential dependence of NO_3^- adsorption and NO_3^* dissociation as a function of catalyst composition is important for understanding the electrocatalytic reduction of nitrate. Herein, we analyzed NO_3^- adsorption and NO_3^* dissociation on pure metals and stable and meta-stable Cu-based single-atom alloy (SAAs) catalysts using both analytical and explicit GC-DFT. We demonstrated that the potential dependence of NO_3^- adsorption and dissociation is linearly dependent on the change in the surface normal dipole moment along the reaction coordinate. Additionally, the electrosorption valencies for NO_3^- adsorption changes across catalysts ranging from $-0.60 \frac{\text{eV}}{\text{V}}$ to $-0.80 \frac{\text{eV}}{\text{V}}$, which correlates with the extent of charge transfer to the surface. The electrosorption valencies for the studied SAAs were generally found to be a weighted average of the electrosorption valencies of the pure Cu host and the pure dopant surface. In contrast, the computed symmetry factors for direct NO_3^* dissociation to nitrite indicate a small potential dependence for this reaction step across all catalysts ($-0.04 \frac{\text{eV}}{\text{V}}$ to $-0.20 \frac{\text{eV}}{\text{V}}$) with no clear relation to charge transfer to or from the surface. Furthermore, trends in the symmetry factors of the SAAs are not well understood by examining the potential dependence or properties of the pure metals.

Across all SAAs, $\text{Ni}_1\text{Cu}(111)$ maintains moderate stability and activity for nitrate adsorption and dissociation. Errors from neglecting the EDL effects for Ni_1Cu range between 5.9 kJ/mol to 61.9 kJ/mol and 3.8 kJ/mol to 51.1 kJ/mol at -0.55 V when either using the Computational Hydrogen Electrode model for NO_3^- adsorption or neglecting the potential dependence for NO_3^* dissociation. However, these values can change with the double-layer properties and catalysts. These results demonstrate the importance of considering EDL effects when modeling the electrocatalytic reduction of nitrate.

Data Availability

Data referenced in the main text, including figures, are tabulated in the SI. Other data, including optimized structures and simulation input files, can be found at the GitHub link.

References

- (1) Wei, M.; Li, S.; Wang, X.; Zuo, G.; Wang, H.; Meng, X.; Wang, J. A Perspective on Cu-Based Electrocatalysts for Nitrate Reduction for Ammonia Synthesis. *Advanced Energy and Sustainability Research* **2024**, *5*, 2300173.
- (2) Wang, Z.; Richards, D.; Singh, N. Recent discoveries in the reaction mechanism of heterogeneous electrocatalytic nitrate reduction. *Catalysis Science & Technology* **2021**, *11*, 705–725, Publisher: The Royal Society of Chemistry.
- (3) Liu, J.-X.; Richards, D.; Singh, N.; Goldsmith, B. R. Activity and Selectivity Trends in Electrocatalytic Nitrate Reduction on Transition Metals. *ACS Catalysis* **2019**, *9*, 7052–7064, Publisher: American Chemical Society.
- (4) Pérez-Gallent, E.; Figueiredo, M. C.; Katsounaros, I.; Koper, M. T. M. Electrocatalytic reduction of Nitrate on Copper single crystals in acidic and alkaline solutions. *Electrochimica Acta* **2017**, *227*, 77–84.
- (5) Giannakakis, G.; Flytzani-Stephanopoulos, M.; Sykes, E. C. H. Single-Atom Alloys as a Reductionist Approach to the Rational Design of Heterogeneous Catalysts. *Accounts of Chemical Research* **2019**, *52*, 237–247, Publisher: American Chemical Society.
- (6) Gao, D.; Yi, D.; Xia, J.; Yang, Y.; Wang, X. First-principles screening of Cu-based single-atom alloys for highly efficient electrocatalytic nitrogen reduction. *Molecular Catalysis* **2024**, *555*, 113879.

- (7) Xing, F.; Jeon, J.; Toyao, T.; Shimizu, K.-i.; Furukawa, S. A Cu–Pd single-atom alloy catalyst for highly efficient NO reduction. *Chemical Science* **2019**, *10*, 8292–8298.
- (8) Wang, S.; Li, L.; Hui, K. S.; Dinh, D. A.; Lu, Z.; Zhang, Q.; Hui, K. N. Non–noble single–atom alloy for electrocatalytic nitrate reduction using hierarchical high–throughput screening. *Nano Energy* **2023**, *113*, 108543.
- (9) Zhang, Y.; Chen, X.; Wang, W.; Yin, L.; Crittenden, J. C. Electrocatalytic nitrate reduction to ammonia on defective Au₁Cu (111) single-atom alloys. *Applied Catalysis B: Environmental* **2022**, *310*, 121346.
- (10) Da, Y.; Jiang, R.; Tian, Z.; Han, X.; Chen, W.; Hu, W. The applications of single-atom alloys in electrocatalysis: Progress and challenges. *SmartMat* **2023**, *4*, e1136, eprint: <https://onlinelibrary.wiley.com/doi/pdf/10.1002/smm2.1136>.
- (11) Yin, H.; Peng, Y.; Li, J. Electrocatalytic Reduction of Nitrate to Ammonia via a Au/Cu Single Atom Alloy Catalyst. *Environmental Science & Technology* **2023**, *57*, 3134–3144, Publisher: American Chemical Society.
- (12) Cai, J.; Wei, Y.; Cao, A.; Huang, J.; Jiang, Z.; Lu, S.; Zang, S.-Q. Electrocatalytic nitrate-to-ammonia conversion with ~100% Faradaic efficiency via single-atom alloying. *Applied Catalysis B: Environmental* **2022**, *316*, 121683.
- (13) Darby, M. T.; Réocreux, R.; Sykes, E. C. H.; Michaelides, A.; Stamatakis, M. Elucidating the Stability and Reactivity of Surface Intermediates on Single-Atom Alloy Catalysts. *ACS Catalysis* **2018**, *8*, 5038–5050, Publisher: American Chemical Society.
- (14) Hannagan, R. T.; Giannakakis, G.; Flytzani-Stephanopoulos, M.; Sykes, E. C. H. Single-Atom Alloy Catalysis. *Chemical Reviews* **2020**, *120*, 12044–12088, Publisher: American Chemical Society.

- (15) Yang, X.-F.; Wang, A.; Qiao, B.; Li, J.; Liu, J.; Zhang, T. Single-Atom Catalysts: A New Frontier in Heterogeneous Catalysis. *Accounts of Chemical Research* **2013**, *46*, 1740–1748, Publisher: American Chemical Society.
- (16) Schumann, J.; Stamatakis, M.; Michaelides, A.; Réocreux, R. Ten-electron count rule for the binding of adsorbates on single-atom alloy catalysts. *Nature Chemistry* **2024**, 1–6, Publisher: Nature Publishing Group.
- (17) Darby, M. T.; Stamatakis, M.; Michaelides, A.; Sykes, E. C. H. Lonely Atoms with Special Gifts: Breaking Linear Scaling Relationships in Heterogeneous Catalysis with Single-Atom Alloys. *The Journal of Physical Chemistry Letters* **2018**, *9*, 5636–5646, Publisher: American Chemical Society.
- (18) Gupta, S.; Rivera, D. J.; Shaffer, M.; Chismar, A.; Muhich, C. Behavior of Cupric Single Atom Alloy Catalysts for Electrochemical Nitrate Reduction: An Ab Initio Study. *ACS ES&T Engineering* **2024**, *4*, 166–175, Publisher: American Chemical Society.
- (19) Nørskov, J. K.; Rossmeisl, J.; Logadottir, A.; Lindqvist, L.; Kitchin, J. R.; Bligaard, T.; Jónsson, H. Origin of the Overpotential for Oxygen Reduction at a Fuel-Cell Cathode. *The Journal of Physical Chemistry B* **2004**, *108*, 17886–17892, Publisher: American Chemical Society.
- (20) Ringe, S.; Hörmann, N. G.; Oberhofer, H.; Reuter, K. Implicit Solvation Methods for Catalysis at Electrified Interfaces. *Chemical Reviews* **2022**, *122*, 10777–10820, Publisher: American Chemical Society.
- (21) Sebastián-Pascual, P.; Shao-Horn, Y.; Escudero-Escribano, M. Toward understanding the role of the electric double layer structure and electrolyte effects on well-defined interfaces for electrocatalysis. *Current Opinion in Electrochemistry* **2022**, *32*, 100918.
- (22) Li, P.; Jiao, Y.; Huang, J.; Chen, S. Electric Double Layer Effects in Electrocatalysis:

- Insights from Ab Initio Simulation and Hierarchical Continuum Modeling. *JACS Au* **2023**, *3*, 2640–2659, Publisher: American Chemical Society.
- (23) Hörmann, N. G.; Beinlich, S. D.; Reuter, K. Converging Divergent Paths: Constant Charge vs Constant Potential Energetics in Computational Electrochemistry. *The Journal of Physical Chemistry C* **2024**, *128*, 5524–5531, Publisher: American Chemical Society.
- (24) Schwarz, K.; Sundararaman, R. The electrochemical interface in first-principles calculations. *Surface science reports* **2020**, *75*, 10.1016/j.surfrep.2020.100492.
- (25) Domínguez-Flores, F.; Melander, M. M. Approximating constant potential DFT with canonical DFT and electrostatic corrections. *The Journal of Chemical Physics* **2023**, *158*, 144701.
- (26) Jinnouchi, R. Grand-Canonical First Principles-Based Calculations of Electrochemical Reactions. *Journal of The Electrochemical Society* **2024**, *171*, 096502, Publisher: IOP Publishing.
- (27) Melander, M. M.; Wu, T.; Weckman, T.; Honkala, K. Constant inner potential DFT for modelling electrochemical systems under constant potential and bias. *npj Computational Materials* **2024**, *10*, 1–11, Publisher: Nature Publishing Group.
- (28) Beinlich, S. D.; Kastlunger, G.; Reuter, K.; Hörmann, N. G. Controlled Electrochemical Barrier Calculations without Potential Control. *Journal of Chemical Theory and Computation* **2023**, *19*, 8323–8331, Publisher: American Chemical Society.
- (29) Sundararaman, R.; Letchworth-Weaver, K.; Schwarz, K. A.; Gunceler, D.; Ozhables, Y.; Arias, T. A. JDFTx: Software for joint density-functional theory. *SoftwareX* **2017**, *6*, 278–284.

- (30) Tran, B.; Goldsmith, B. R. Theoretical Investigation of the Potential-Dependent CO Adsorption on Copper Electrodes. *The Journal of Physical Chemistry Letters* **2024**, *15*, 6538–6543, Publisher: American Chemical Society.
- (31) Wong, A. J.-W.; Tran, B.; Agrawal, N.; Goldsmith, B. R.; Janik, M. J. Sensitivity Analysis of Electrochemical Double Layer Approximations on Electrokinetic Predictions: Case Study for CO Reduction on Copper. *The Journal of Physical Chemistry C* **2024**, Publisher: American Chemical Society.
- (32) Clary, J. M.; Vigil-Fowler, D. Adsorption Site Screening on a PGM-Free Electrocatalyst: Insights from Grand Canonical Density Functional Theory. *The Journal of Physical Chemistry C* **2023**, *127*, 16405–16413.
- (33) Alsunni, Y. A.; Alherz, A. W.; Musgrave, C. B. Electrocatalytic Reduction of CO₂ to CO over Ag(110) and Cu(211) Modeled by Grand-Canonical Density Functional Theory. *The Journal of Physical Chemistry C* **2021**, *125*, 23773–23783, Publisher: American Chemical Society.
- (34) Hörmann, N. G.; Marzari, N.; Reuter, K. Electrosorption at metal surfaces from first principles. *npj Computational Materials* **2020**, *6*, 1–10, Publisher: Nature Publishing Group.
- (35) Janak, J. F. Proof that $\frac{\partial E}{\partial n_i} = \epsilon_i$ in density-functional theory. *Physical Review B* **1978**, *18*, 7165–7168, Publisher: American Physical Society.
- (36) Guo, Y.; Sun, N.; Luo, L.; Cheng, X.; Chen, X.; Yan, X.; Shen, S.; Zhang, J. Potential-dependent insights into the origin of high ammonia yield rate on copper surface via nitrate reduction: A computational and experimental study. *Journal of Energy Chemistry* **2024**, *96*, 272–281.

- (37) Agrawal, N.; Wong, A. J.-W.; Maheshwari, S.; Janik, M. J. An efficient approach to compartmentalize double layer effects on kinetics of interfacial proton-electron transfer reactions. *Journal of Catalysis* **2024**, *430*, 115360.
- (38) Cui, Z.; Wong, A. J.-W.; Janik, M. J.; Co, A. C. Negative Reaction Order for CO during CO₂ Electroreduction on Au. *Journal of the American Chemical Society* **2024**, *146*, 23872–23880, Publisher: American Chemical Society.
- (39) Gauthier, J. A.; Ringe, S.; Dickens, C. F.; Garza, A. J.; Bell, A. T.; Head-Gordon, M.; Nørskov, J. K.; Chan, K. Challenges in Modeling Electrochemical Reaction Energetics with Polarizable Continuum Models. *ACS Catalysis* **2019**, *9*, 920–931, Publisher: American Chemical Society.
- (40) Darby, M. T.; Sykes, E. C. H.; Michaelides, A.; Stamatakis, M. Carbon Monoxide Poisoning Resistance and Structural Stability of Single Atom Alloys. *Topics in Catalysis* **2018**, *61*, 428–438.
- (41) Papanikolaou, K. G.; Darby, M. T.; Stamatakis, M. CO-Induced Aggregation and Segregation of Highly Dilute Alloys: A Density Functional Theory Study. *The Journal of Physical Chemistry C* **2019**, *123*, 9128–9138, Publisher: American Chemical Society.
- (42) Salem, M.; Cowan, M. J.; Mpourmpakis, G. Predicting Segregation Energy in Single Atom Alloys Using Physics and Machine Learning. *ACS Omega* **2022**, *7*, 4471–4481, Publisher: American Chemical Society.
- (43) Salem, M.; Loevlie, D. J.; Mpourmpakis, G. Single Atom Alloys Segregation in the Presence of Ligands. *The Journal of Physical Chemistry C* **2023**, *127*, 22790–22798, Publisher: American Chemical Society.
- (44) Hammer, B.; Hansen, L. B.; Nørskov, J. K. Improved adsorption energetics within density-functional theory using revised Perdew-Burke-Ernzerhof functionals. *Physical Review B* **1999**, *59*, 7413–7421, Publisher: American Physical Society.

- (45) Wang, Z.; Jiao, D.; Zhao, J. A direct complete dissociation mechanism for nitrate reaction to ammonia. *Molecular Catalysis* **2024**, *552*, 113692.
- (46) Richards, D.; D. Young, S.; R. Goldsmith, B.; Singh, N. Electrocatalytic nitrate reduction on rhodium sulfide compared to Pt and Rh in the presence of chloride. *Catalysis Science & Technology* **2021**, *11*, 7331–7346, Publisher: Royal Society of Chemistry.
- (47) Islam, S. M. R.; Khezeli, F.; Ringe, S.; Plaisance, C. An implicit electrolyte model for plane wave density functional theory exhibiting nonlinear response and a nonlocal cavity definition. *The Journal of Chemical Physics* **2023**, *159*, 234117.
- (48) Leung, T. C.; Kao, C. L.; Su, W. S.; Feng, Y. J.; Chan, C. T. Relationship between surface dipole, work function and charge transfer: Some exceptions to an established rule. *Physical Review B* **2003**, *68*, 195408, Publisher: American Physical Society.
- (49) Schmickler, W.; Guidelli, R. The partial charge transfer. *Electrochimica Acta* **2014**, *127*, 489–505.
- (50) Rusu, P. C.; Brocks, G. Surface Dipoles and Work Functions of Alkylthiolates and Fluorinated Alkylthiolates on Au(111). *The Journal of Physical Chemistry B* **2006**, *110*, 22628–22634, Publisher: American Chemical Society.
- (51) Hofmann, O. T.; Atalla, V.; Moll, N.; Rinke, P.; Scheffler, M. Interface dipoles of organic molecules on Ag(111) in hybrid density-functional theory. *New Journal of Physics* **2013**, *15*, 123028, Publisher: IOP Publishing.
- (52) Otero, R.; Vázquez De Parga, A.; Gallego, J. Electronic, structural and chemical effects of charge-transfer at organic/inorganic interfaces. *Surface Science Reports* **2017**, *72*, 105–145.
- (53) Limas, N. G.; Manz, T. A. Introducing DDEC6 atomic population analysis: part 4. Efficient parallel computation of net atomic charges, atomic spin moments, bond or-

ders, and more. *RSC Advances* **2018**, *8*, 2678–2707, Publisher: The Royal Society of Chemistry.

- (54) Patel, D. A.; Hannagan, R. T.; Kress, P. L.; Schilling, A. C.; Çınar, V.; Sykes, E. C. H. Atomic-Scale Surface Structure and CO Tolerance of NiCu Single-Atom Alloys. *The Journal of Physical Chemistry C* **2019**, *123*, 28142–28147, Publisher: American Chemical Society.

Acknowledgments

The authors would like to thank the National Science Foundation for providing funding support for this research via the CAREER Award 2236138.

Author Contributions

D.S. wrote the initial manuscript draft, performed all computational studies, and was responsible for data collection and analysis. B.T. reviewed/edited the manuscript and advised D.S. on all computational studies. B.G. reviewed/edited the manuscript, advised D.S. on all computational studies, and conceived the original work.

Competing Interests

The authors declare no conflict of interest.